The dehydration of $SrTeO_3(H_2O)$ - a topotactic reaction for preparation of the new metastable strontium oxotellurate(IV) phase ε-$SrTeO_3$†

Berthold Stöger,[a] Matthias Weil,*[a] Enrique J. Baran,[b] Ana C. González-Baró,[b] Sylvie Malo,[c] Jean Michel Rueff,[c] Sebastien Petit,[c] Marie Bernadette Lepetit,[c] Bernard Raveau[c] and Nicolas Barrier*[c]

Microcrystalline single-phase strontium oxotellurate(IV) monohydrate, $SrTeO_3(H_2O)$, was obtained by microwave-assisted hydrothermal synthesis under alkaline conditions at 180 °C for 30 min. A temperature of 220 °C and longer reaction times led to single crystal growth of this material. The crystal structure of $SrTeO_3(H_2O)$ was determined from single crystal X-ray diffraction data: $P2_1/c$, $Z = 4$, $a = 7.7669(5)$, $b = 7.1739(4)$, $c = 8.3311(5)$ Å, $\beta = 107.210(1)°$, $V = 443.42(5)$ Å^3, 1403 structure factors, 63 parameters, $R[F^2 > 2\sigma(F^2)] = 0.0208$, $wR(F^2$ all$) = 0.0516$, $S = 1.031$. $SrTeO_3(H_2O)$ is isotypic with the homologous $BaTeO_3(H_2O)$ and is characterised by a layered assembly parallel to (100) of edge-sharing $[SrO_6(H_2O)]$ polyhedra capped on each side of the layer by trigonal-prismatic $[TeO_3]$ units. The cohesion of the structure is accomplished by moderate O–H$\cdots$O hydrogen bonding interactions between donor water molecules and acceptor O atoms of adjacent layers. In a topochemical reaction, $SrTeO_3(H_2O)$ condensates above 150 °C to the metastable phase ε-$SrTeO_3$ and transforms upon further heating to δ-$SrTeO_3$. The crystal structure of ε-$SrTeO_3$, the fifth known polymorph of this composition, was determined from combined electron microscopy and laboratory X-ray powder diffraction studies: $P2_1/c$, $Z = 4$, $a = 6.7759(1)$, $b = 7.2188(1)$, $c = 8.6773(2)$ Å, $\beta = 126.4980(7)°$, $V = 341.20(18)$ Å^3, $R_{Fobs} = 0.0166$, $R_{Bobs} = 0.0318$, $Rwp = 0.0733$, $Goof = 1.38$. The structure of ε-$SrTeO_3$ shows the same basic set-up as $SrTeO_3(H_2O)$, but the layered arrangement of the hydrous phase transforms into a framework structure after elimination of water. The structural studies of $SrTeO_3(H_2O)$ and ε-$SrTeO_3$ are complemented by thermal analysis and vibrational spectroscopic measurements.

1 Introduction

The market for materials exhibiting ferroelectric or nonlinear optical (NLO) properties is steadily growing. The underlying compounds have extensive technical applications in the fields of capacitors, lasers, frequency-doubling and other electric and optical devices. The basic prerequisite for such a class of compounds is a non-centrosymmetric crystal structure and the presence of a high polarisability. Ions with non-bonded *s*-electrons such as Sn^{II}, Sb^{III}, Pb^{II}, Tl^{I} or Bi^{III} have a strong preference for a peculiar stereochemistry and are frequently found in an asymmetric environment in the crystal structures due to formation of $[MY_nE]$ polyhedra missing a centre of symmetry (M is the cationic, Y is the anionic component and E denotes the electron lone pair). Other potential building blocks for crystal engineering of such materials are oxoanions of the type XO_3^{n-} ($X = As^{III}$, S^{IV}, Te^{IV}, Se^{IV}), resulting in strongly distorted XO_3E polyhedra. For various technological applications the desired materials must have both chemical and thermal stability over a wide temperature range, ruling out most of the oxoarsenate(III), oxosulfate(IV) and oxoselenate(IV) compounds which are all strongly prone to hydrolysis, oxidation or premature thermal decomposition. The most promising behaviour with respect to the desired stability ranges of the above mentioned compounds is shown by metal oxotellurates(IV), in particular by the heavier alkaline earth elements with formula $MTeO_3$ (M = Ca, Sr, Ba).

In fact, $CaTeO_3$ and $SrTeO_3$ show ferroelectric properties.[1–3] Numerous studies have been performed on single crystal growth and measurements of physical properties of $CaTeO_3$ and $SrTeO_3$, including ferroelectric, piezoelectric and optical behaviour,[4] dielectric[5] and optical properties,[6] electric conductivity,[7] and phase transition points.[8] Nevertheless, the corresponding crystal structures of the polymorphic $MTeO_3$ phases were determined only recently for $M = $ Ca[9] and $M = $ Sr.[10–13] In the majority of cases, these $MTeO_3$ ($M = $ Ca, Sr) phases were prepared

[a]*Institute for Chemical Technologies and Analytics, Division of Structural Chemistry, Vienna University of Technology, Getreidemarkt 9/164-SC, A-1060, Vienna, Austria*
[b]*Centro de Química Inorgánica (CEQUINOR, CONICET/UNLP), Facultad de Ciencias Exactas, Universidad Nacional de La Plata, C. Correo 962, 1900, La Plata, Argentina*
[c]*Laboratoire CRISMAT, UMR 6508 CNRS ENSICAEN, 6 bd Maréchal Juin, 14050, CAEN Cedex 4, France*
† ICSD reference numbers 422355 and 422356.

by typical solid state reactions with TeO_2 and corresponding alkaline earth carbonates as reagents. Since at the required temperatures (> 800 °C) TeO_2 has a noticeable vapour pressure and can be oxidized under atmospheric conditions to Te(VI), the reaction control for preparation of single phase products is relatively complex. A more suitable method for the preparation of microcrystalline $MTeO_3$ (M = Ca, Sr) phases makes use of the dehydration reaction of corresponding $MTeO_3(H_2O)$ phases at comparatively low temperatures ("chimie douce" reaction route)[14] and has originally been applied for preparation of $CaTeO_3$[15] and $SrTeO_3$.[16] However, when we made use of this method to prepare microcrystalline $SrTeO_3$ by thermal decomposition of $SrTeO_3(H_2O)$ at temperatures above 350 °C, we obtained a powder X-ray diffraction pattern whose lines could neither be indexed on basis of the crystal structures of one of the four known $SrTeO_3$ polymorphs[10–13] nor of any other known phase in the system Sr–Te–O, viz. $Sr_3Te_4O_{11}$,[17] $SrTe_5O_{11}$,[18] $SrTeO_4$[19] or $SrTe_3O_8$.[20]

We therefore attempted to determine the crystal structure of the obtained decomposition product from X-ray powder data and were eventually able to show that it is in fact the fifth $SrTeO_3$ polymorph which we will denote in the following as ε-$SrTeO_3$. In this communication we also report on preparation, crystal structure determination, thermal analysis and vibrational spectra of the hydrous phase $SrTeO_3(H_2O)$ which was employed as the precursor material for preparation of ε-$SrTeO_3$.

2 Experimental

2.1 Synthesis of SrTeO₃(H₂O)

2.1.1 Microcrystalline material.

-by precipitation. The reagent Na_2TeO_3 was prepared according to Brauer[21] by melting stoichiometric amounts of TeO_2 and Na_2CO_3 at 800 °C. In a typical experiment for preparation of $SrTeO_3(H_2O)$, a solution of 378 mg (1.3 mmol) $Sr(NO_3)_2$ in 20 mL water was added to a solution of 353 mg (1.4 mmol) Na_2TeO_3 in 10 mL water which resulted in an instant precipitation of a slightly off-white solid. The suspension was boiled for ten minutes, and the precipitate was then filtered off and subsequently washed with mother liquor and acetone, and was finally dried in a desiccator overnight. As can be seen from scanning electron microscopy images (Fig. 1a), the peculiar feature of the microcrystalline product is the very thin sheet-like form of the crystals which assemble into rosebud-like agglomerates. This was also noted in the powder diffraction pattern that shows a pronounced preferred orientation along [100].

-by hydrothermal microwave-assisted synthesis. Microcrystalline $SrTeO_3(H_2O)$ has also been obtained by microwave-assisted hydrothermal synthesis using a MARS 5 CEM μ Waves Digestion System according to the following procedure. In a Teflon-lined autoclave (XP1500+) one equivalent of strontium nitrate ($Sr(NO_3)_2$, 1.326 g, 6.27 mmol), one equivalent of tellurium dioxide (TeO_2, 1 g, 6.27 mmol) and three equivalents of sodium hydroxide (NaOH, 0.752 g, 18.8 mmol) were mixed in 30 mL of distilled water. The autoclave was then heated from room temperature to 180 °C in 30 min with a selected power of 400 W, held at this temperature at the same power during 5 h and was finally cooled to room temperature within 30 min. The final compound $SrTeO_3(H_2O)$ was obtained as a pure microcrystalline white powder and was
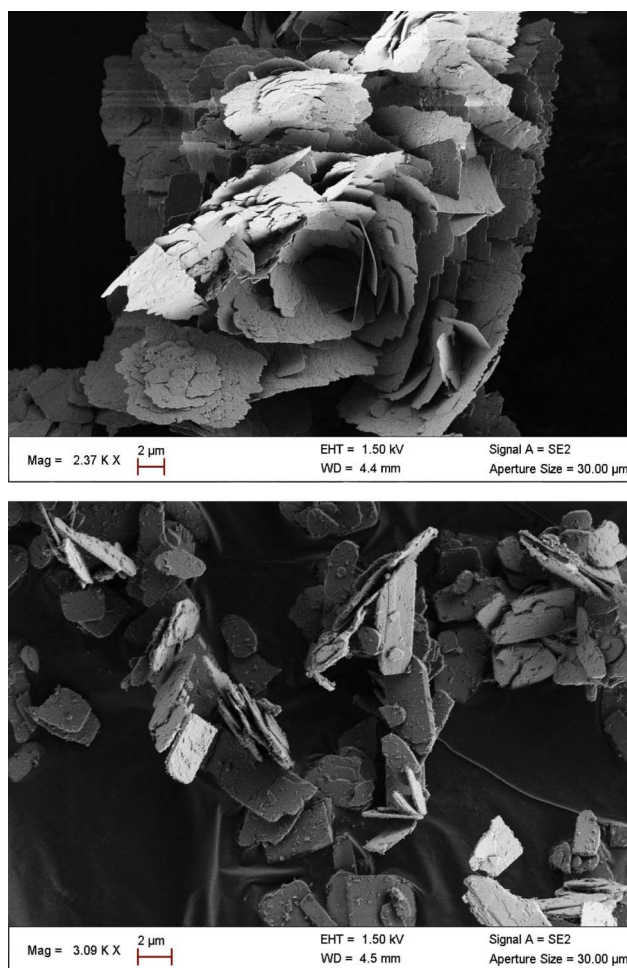

| Mag = 2.37 K X | 2 µm | EHT = 1.50 kV | Signal A = SE2 |
| | | WD = 4.4 mm | Aperture Size = 30.00 µm |

| Mag = 3.09 K X | 2 µm | EHT = 1.50 kV | Signal A = SE2 |
| | | WD = 4.5 mm | Aperture Size = 30.00 µm |

Fig. 1 Typical views of the forms of microcrystalline $SrTeO_3(H_2O)$ as observed by scanning electron microscopy: platy crystals forming rosebud–like agglomerates and obtained from precipitation (top); plate-like crystals obtained from microwave-assisted hydrothermal synthesis (bottom).

filtered off, washed with water, rinsed with ethanol and dried in air. The crystallites showed likewise a plate-like form (Fig. 1b) but appear thicker than those obtained from precipitation.

2.1.2 Single crystal material.
Hydrothermal treatment of a mixture of 221 mg Na_2TeO_3 and 267 mg $SrCl_2·6H_2O$ in 3 mL of an aqueous $20\%_{wt}$ NH_4OH solution in a Teflon-lined autoclave at 220 °C for one week yielded different phases in single crystalline form. Besides black needles of elementary tellurium, colourless blocks of $Sr_3Te_4O_{11}$[17] and colourless plates and blocks of $SrTeO_3(H_2O)$ were obtained. The crystals were separated under a polarising microscope and their composition determined by single crystal diffraction. Phase analysis based on XRPD data of the ground bulk material revealed an approximate phase composition of $42\%_{wt}$ $SrTeO_3(H_2O)$, $53\%_{wt}$ $Sr_3Te_4O_{11}$ and $5\%_{wt}$ Te. Some additional weak reflections could not be assigned to any known phase.

2.1.2 Synthesis of ε-SrTeO₃.
Microcrystalline ε-$SrTeO_3$ was prepared *in situ* by dehydration of $SrTeO_3(H_2O)$ (obtained from the hydrothermal microwave-assisted reaction route) at 390 °C under vacuum for 4 h in a Anton Paar HTK1200N high temperature chamber. At this temperature a sufficient quantity

of the dehydrated phase with a reasonable crystallinity necessary for subsequent structure refinements based on electron diffraction and Rietveld refinement could be prepared.

2.2 Electron microscopy

Electron diffraction (ED) studies of microcrystalline $SrTeO_3$ were carried out with a JEOL 200CX electron microscope fitted with an eucentric goniometer ($\pm$ 60°) and equipped with an energy dispersive spectroscopy (EDS) analyzer. For the transmission electron microscopy studies, the samples were reground in alcohol and deposited on a perforated carbon membrane supported by a copper grid. Simulations of ED patterns were calculated with the JEMS v3.4705U2009 software.[22]

Scanning electron microscopy (SEM) was performed using a Zeiss supra 55 electron microscope. The Sr : Te ratio was determined by energy-dispersive X-ray spectroscopy (EDS) analyses on numerous crystallites and was close to the nominal composition.

2.3 Thermal analysis

Thermogravimetric (TG) and differential scanning calorimetry (DSC) measurements were carried out with a heating rate of 10 K min^{-1} in a flowing nitrogen atmosphere (20 mL min^{-1}). For the TG measurements, a NETZSCH TG 209 F9 Tarsus system, working with open aluminium oxide crucibles, was used. For the DSC measurements, a NETZSCH DSC 200 F3 Maia and a Mettler-Toledo DSC 25 system, both working with aluminium pans with pierced lids, were employed.

2.4 X-ray diffraction

2.4.1 Single crystal X-ray diffraction of $SrTeO_3(H_2O)$.
Single crystals suitable for the X-ray studies were pre-selected under a polarizing microscope. Intensity measurements were then performed at room temperature on a Bruker SMART-CCD area diffractometer system, using Mo-Kα radiation and a graphite monochromator. For the finally selected crystal, a complete reciprocal sphere up to 62°/2θ was recorded. Intensity data were processed with the SMART and SAINT software,[23] and absorption effects were corrected using the SADABS algorithm that is based on a multi-scan approach.[24] The crystal structure of $SrTeO_3(H_2O)$ was solved with direct methods and was subsequently refined with full-matrix least-squares refinements on F^2 with the SHELXTL software suite.[25] In the final refinement cycles, the displacement parameters of all non-H atoms were refined anisotropically. The protons of the water molecule were clearly discernible from difference maps. Their positions were refined with distance restraints of d (O–H $\neq$ 0.95 Å and d(H$\cdots$H) = 1.50 Å and a common U_{iso}(H) parameter. The largest residual electron density peaks in the final difference map were inconspicuous, indicating no additional atomic sites.

2.4.2 X-ray powder diffraction and crystal structure determination of ε-$SrTeO_3$.
X-ray powder diffraction patterns were collected on a Bruker D8 diffractometer using Cu-Kα_1 radiation (1.54056 Å), selected by an incident germanium monochromator, and equipped with a Lynx-Eye detector and an Anton Paar HTK1200N high temperature chamber. At room temperature (without mounting the high-temperature chamber) the diagrams were collected in a continuous scan mode with a step scan of ~0.009°/2θ ranging from 5 to 140°/2θ. Diagrams from the temperature-dependent diffraction experiments were collected under primary vacuum (~ 8.10^{-3} mbar) using a step scan of ~0.014°/2θ ranging from 9 to 80°/2θ, and were recorded every 20 °C between 30° and 610 °C.

The electron diffraction measurements were carried out at room temperature. The reconstruction of the reciprocal space, done by tilting around crystallographic axes, evidenced a monoclinic symmetry with at least a screw axis. The pronounced preferred orientation of the crystallites did not allow recording all the basic planes. Nonetheless, the derived monoclinic unit cell characterized by $a \approx 6.8$ Å, $b \approx 7.1$ Å, $c \approx 8.7$ Å and $\beta \approx 127°$, without any reflection conditions, allowed to index all the ED patterns observed (Fig. 2a–c).
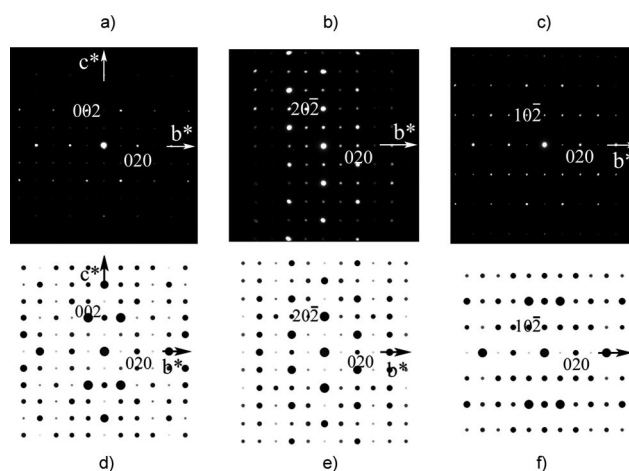

Fig. 2 ε-$SrTeO_3$: Experimental ED patterns recorded at room temperature along a) [100] b) [101] c) [201], and simulated ED patterns with the structural model determined from XRPD considering double diffraction along (d) [100], (e) [101], and (f) [201].

The structure of ε-$SrTeO_3$ was solved from room temperature X-ray powder diffraction data. A first pattern matching of the experimental X-ray powder diffraction diagram on the basis of the cell as determined from electron diffraction studies was performed with the program JANA2006[26] in space group $P2$. A careful observation of the indexed pattern showed that all ($0k0$) reflections with $k = 2n+1$ and all ($h0l$) reflections with $l = 2n+1$ are systematically absent. These reflection conditions are consistent with space group $P2_1/c$. It should be noted that two weak reflections at 25.16°/2θ and 25.81°/2θ could not be indexed and presumably correspond to small amounts of an yet unidentified by-product. The extraction of the structure factors using the Le Bail method[27] was carried out with JANA2006. The structure was solved using Endeavour.[28] The best solution was obtained with a reliability factor of $R_F = 0.301$ and all positions of the Sr, Te and O atoms were directly found. Subsequent Rietveld refinements of this model were performed with JANA2006. Preferred orientation of reflections along the [100] axis was corrected assuming a March and Dollase function.[29] The refined preferred orientation parameter is 0.690(7) which is consistent with the plate-like crystallite form (Fig. 1). Anisotropic strain broadening of peaks was corrected by the tensor method[30] and peak asymmetry due to axial divergence was also corrected according to the Finger,
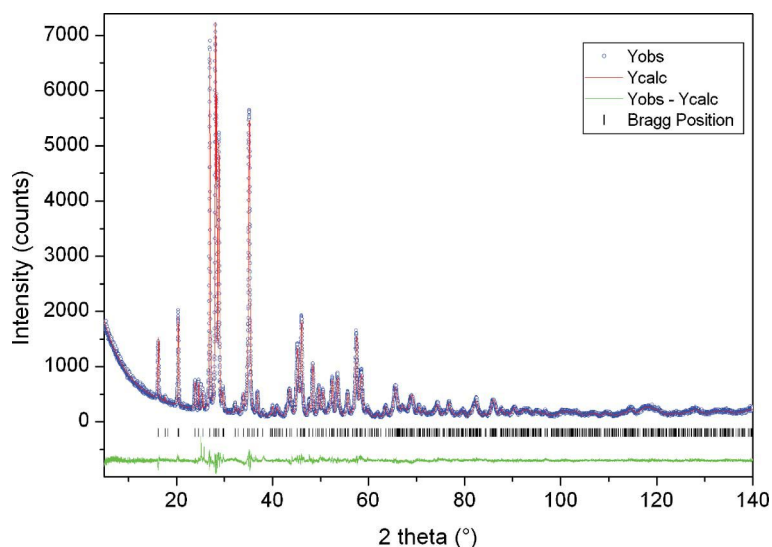
Fig. 3 X-ray powder diffraction pattern of ε-SrTeO$_3$ (Cu–K$_{α1}$ radiation; 1.5406 Å), with observed (dots), calculated (solid line), Bragg reflections (ticks) and difference profiles obtained after Rietveld refinement.

Table 1 SrTeO$_3$(H$_2$O). Details of single crystal data collection and structure refinement

Diffractometer	SMART CCD (Siemens)
Radiation; λ/Å	Mo K$\bar{\alpha}$; 0.71073
T/°C	22(1)
Crystal dimensions/mm	$0.120 \times 0.072 \times 0.024$
Crystal color; shape	colourless block
Space group, no.	$P2_1/c$, 14
Formula units Z	4
a/Å	7.7669(5)
b/Å	7.1739(4)
c/Å	8.3311(5)
β/°	107.210(1)
V/Å^3	443.42(5)
Formula weight	281.24
μ/mm^{-1}	18.485
X-ray density/g cm^{-3}	4.213
Range θ_{min}–θ_{max}	2.75–31.00
Range	
h	$-11 \rightarrow 11$
k	$-10 \rightarrow 10$
l	$-12 \rightarrow 11$
Measured reflections	4956
Independent reflections	1403
Obs. reflections [$I > 2\sigma(I)$]	1320
R_{int}	0.033
Absorption correction	SADABS
Trans. coef. T_{min}; T_{max}	0.2151; 0.6653
Number of parameters	63
Ext. coef. (SHELXL97)	0.0019(4)
Diff. elec. dens. max; min	1.22 (0.76, Te);
[e$^-$ Å^{-3}] (dist./Å, atom)	-1.30 (1.14, Te)
$R[F^2 > 2\sigma(F^2)]$	0.0208
w$R_2(F^2$ all)	0.0516
Goof	1.031
CSD number	422355

Table 2 ε-SrTeO$_3$. Details of X-ray powder diffraction data and structure refinement

Diffractometer	Bruker D8 advance vario1
Radiation; λ/Å	Cu-Kα_1 radiation/1.5406
Angular range/°2θ	5–140
Step size/°2θ	0.009
T/°C	20(1)
Pref. orient. correction	March & Dollase - along [100]
Asymmetry correction	axial divergence - Finger, Cox & Jephcoat
Anisotropic strain broadering	Stephens
Space group, no.	$P2_1/c$, 14
Formula units Z	4
a/Å	6.7759(1)
b/Å	7.2188(1)
c/Å	8.6773(2)
β (°)	126.4980(7)
V/Å^3	341.20(18)
Formula weight	263.22
X-ray density/g cm^{-3}	5.122
Rietveld agreement indices	
profile, Rp	0.0512
weighted profile, Rwp	0.0733
background	12 Legendre polynoms
corrected profile, cRp	0.0948
derived Bragg R-factor, R_{Bobs}	0.0318
Goof	1.38
CSD number	422356

dinates and isotropic displacement parameters of the structures of SrTeO$_3$(H$_2$O) and ε-SrTeO$_3$ are given in Table 3, and anisotropic displacement parameters for SrTeO$_3$(H$_2$O) are gathered in Table 4. Selected interatomic distances and angles of the two structures are summarized in Table 5. The structure model of ε-SrTeO$_3$ as determined from XRPD data was used for the calculation of the ED patterns of the basal planes represented in Fig. 2d–f. The variation of the intensity of the spots observed on the experimental ED patterns (Fig. 2a–c) is similar to the one observed on the simulated patterns (Fig. 2d–f), which confirms the validity of the structural model. Drawings of structural details were produced using the software DIAMOND.[32]

Cox & Jephcoat approach.[31] The final refinement converged with reliability factors of R_{Bobs} = 0.0318 and profile factors of Rp = 0.0512; Rwp = 0.073; $Goof$ = 1.38. The resulting X-ray diffraction diagram is shown in Fig. 3.

Further details of the single crystal and powder data collections and refinements are summarized in Tables 1 and 2. Atomic coor-

Table 3 SrTeO$_3$(H$_2$O) and ε-SrTeO$_3$. Atomic coordinates and equivalent isotropic displacement parameters $U_{eq} = (1/3)\Sigma_i\Sigma_j U_{ij}a_i^*a_j^*\mathbf{a}_i\cdot\mathbf{a}_j$/Å^2

Atom	Wyckoff position	x	y	z	U_{eq}
SrTeO$_3$(H$_2$O)					
Te	4 e	0.78482(2)	0.17353(3)	0.50726(2)	0.01131(8)
Sr	4 e	0.39762(4)	0.35827(4)	0.66278(3)	0.01280(8)
O1	4 e	0.5674(3)	0.3052(3)	0.4498(3)	0.0151(4)
O2	4 e	0.6973(3)	−0.0211(3)	0.3564(3)	0.0166(4)
O3	4 e	0.7776(3)	0.0758(3)	0.7117(2)	0.0216(5)
OW	4 e	0.1432(3)	0.4112(4)	0.3855(3)	0.0279(6)
HW1	4 e	0.188(6)	0.440(7)	0.303(5)	0.058(12)
HW2	4 e	0.021(5)	0.414(8)	0.342(6)	0.058(12)
ε-SrTeO$_3$					
Te	4 e	0.37129(14)	0.16973(13)	0.10244(12)	0.0108(4)
Sr	4 e	0.86465(19)	0.37061(15)	0.1324(2)	0.0140(5)
O1	4 e	0.2282(7)	−0.0291(9)	−0.0583(9)	0.010(19)
O2	4 e	0.3892(8)	0.1085(11)	0.3072(11)	0.017(2)
O3	4 e	0.0853(9)	0.1461(10)	0.4851(9)	0.020(2)

Table 4 SrTeO$_3$(H$_2$O). Anisotropic displacement parameters Å^{-2}

Atom	U_{11}	U_{22}	U_{33}	U_{23}	U_{13}	U_{12}
Te	0.01030(11)	0.01264(11)	0.01116(11)	−0.00004(6)	0.00342(7)	−0.00074(6)
Sr	0.01497(14)	0.01133(14)	0.01183(14)	0.00000(8)	0.00356(11)	−0.00026(9)
O1	0.0133(10)	0.0146(10)	0.0177(10)	0.0003(8)	0.0049(8)	0.0027(7)
O2	0.0203(10)	0.0126(10)	0.0167(9)	−0.0016(8)	0.0052(8)	−0.0015(8)
O3	0.0220(11)	0.0294(13)	0.0135(9)	0.0029(9)	0.0052(8)	−0.0059(10)
OW	0.0171(11)	0.0473(17)	0.0176(11)	0.0029(11)	0.0027(9)	−0.0082(11)

Table 5 SrTeO$_3$(H$_2$O) and ε-SrTeO$_3$. Selected interatomic distances (Å) angles (°) for both structures as well as hydrogen bonding interactions for SrTeO$_3$(H$_2$O)

SrTeO$_3$(H$_2$O)

Sr	—	O3	2.495(2)		Te	—	O3	1.858(2)
	—	O2	2.520(2)			—	O2	1.867(2)
	—	O1	2.533(2)			—	O1	1.870(2)
	—	OW	2.586(2)		ø			1.865
	—	O1	2.633(2)			—	OW	3.113(3)
	—	O1	2.639(2)		O3	Te	O2	103.37(9)
	—	O2	2.676(2)		O3	Te	O1	98.95(9)
ø			2.583		O2	Te	O1	94.84(9)
					ø			99.05

D	H	A	D–H	H–A	D–A	∠(DHA)
OW	HW1	O2	0.88(3)	1.83(3)	2.703(3)	173(5)
OW	HW2	O3	0.91(3)	1.88(4)	2.781(3)	169(4)

ε-SrTeO$_3$

Sr	—	O3	2.350(8)		Te	—	O1	1.763(10)
	—	O3	2.481(9)			—	O2	1.827(6)
	—	O2	2.531(6)			—	O3	2.052(6)
	—	O2	2.591(5)		ø			1.881
	—	O1	2.694(9)		O1	Te	O3	102.4(2)
	—	O1	2.748(5)		O1	Te	O2	105.0(3)
	—	O3	2.964(7)		O2	Te	O3	98.1(3)
ø			2.623		ø			101.8

Additional crystallographic information on each structure can be obtained from the Fachinformationszentrum Karlsruhe, D-76344 Eggenstein-Leopoldshafen, Germany, E-mail: crysdata@fiz-karlsruhe.de, by quoting the reference and the CSD-numbers listed at the end of Tables 1 and 2.

2.5 Electronic lone pair localisation

Ab initio calculations based on the Density Functional Theory (DFT) were performed in order to accurately locate the 5s^2 electron lone pairs of the tellurium atoms in both ε-SrTeO$_3$ and SrTeO$_3$(H$_2$O) structures. The electronic structures were calculated

with the CRYSTAL software[33] using the B3LYP approximation, Stuttgart core pseudo-potentials (ECP28MDF) and a valence double zeta basis set for tellurium atoms,[34] Hay-Wadt small-core ECP with a 311(1d)G basis set for strontium atoms,[35] a 8-411(1d)G basis set for oxygen atoms,[35] and 3-1(p)G basis set for hydrogen atoms.[36] The localization of the electron lone pairs was carried out by an electron localization function (ELF) analysis with a code provided by J. Contreras-Garcia.[37] The 3D plots of the ELF were produced with the software vmd.[38]

2.6 Vibrational Spectroscopy

The infrared spectra of microcrystalline $SrTeO_3(H_2O)$ obtained from the microwave-assisted hydrothermal method, were recorded in the spectral range between 4000–400 cm^{-1} with a Bruker IFS 66 FTIR instrument, with the powdered samples dispersed in KBr. Raman spectra were recorded with a FRA 106 Raman accessory of the same instrument, using the 1064 nm line of a Nd:YAG solid state laser for excitation. Far IR spectra were measured with the compound dispersed in polyethylene discs, using a Perkin Elmer System 2000 FTIR instrument.

3 Results and Discussion

3.1 Crystal Structures

$SrTeO_3(H_2O)$ crystallizes isotypically with the structure of the higher homologue $BaTeO_3(H_2O)$.[39]‡ It is built up of distorted $[SrO_6(H_2O)]$ polyhedra and isolated $[Te^{IV}O_3]$ units as the main building blocks (Fig. 4a). The coordination around the alkaline earth cations might be described as an intermediate between a monocapped octahedron and a pentagonal bipyramid with Sr–O distances ranging from 2.495(2) to 2.676(2) Å and an average distance of $\bar{d}$ (Sr–O)= 2.583 Å. The latter compares well with the sum of the ionic radii of 2.59 Å.[40] The $[Te^{IV}O_3]$ unit displays the well-known trigonal-pyramidal geometry of XO_3E groups showing an average distance of $\bar{d}$(Te–O)= 1.865 Å and a mean O–Te–O angle of 99.05°. The next-nearest O atom around the Te atom

is that of the water molecule with a separation of 3.113(3) Å which, owing to the remote distance, is considered as non-bonding.[41]

The $SrTeO_3(H_2O)$ structure can be described as being constructed of edge-sharing $[SrO_6(H_2O)]$ polyhedra forming extended layers parallel to the (100) plane. The isolated $[TeO_3]$ units are attached on each side of these layers which in turn are held together along [100] by O–H$\cdots$O hydrogen bonding interactions at 2.703(3) and 2.781(3) Å between the donor water molecules and acceptor O atoms of the adjacent layers (Table 5). Like in most of the known oxotellurate(IV) structures,[42] the electron lone pairs E are stereochemically active and are situated between the layers (Fig. 5). Under consideration of the space requirement of the electron lone pair E, the environment around tellurium can be described as a distorted $[TeO_3E]$ ψ-tetrahedron. The electron lone pair was located using the electron localization function (ELF) method[37] after performing DFT calculations (see section 2.5). The lone pair points out close to the [100] direction: Te–$E = 0.18458a + 0,0717b + 0.03824c$ (Fig. 5b). The geometric center of the electron lone pair is at a distance of 1.46 Å from the Te atom. The calculated electronic charge associated with the lone pair is equal to 2.22 electrons within a volume of 17.4 Å^3.

The ε-$SrTeO_3$ phase forms in a topotactic dehydration reaction from $SrTeO_3(H_2O)$ above 150 °C (Fig. 4). After elimination of the water molecules that are located at $x \approx \frac{1}{2}$, the layer structure of $SrTeO_3(H_2O)$ is re-organised by condensation of adjacent layers. The novel structure of ε-$SrTeO_3$ is closely related to that of $SrTeO_3(H_2O)$ but shows a considerable distortion of the complete unit cell and in particular of the monoclinic angle (see Tables 1 and 2). Like $SrTeO_3(H_2O)$, this dehydrated form can be described as built up from SrO_7 polyhedra and distorted ψ-$[TeO_3E]$ tetrahedra as main building blocks. The $[TeO_3]$ units exhibit a similar but distorted geometry to that of $SrTeO_3(H_2O)$, with Te–O distances ranging from 1.764(10) to 2.052(6) Å with a mean $\bar{d}$(Te–O) distance and an (O–Te–O) angle of 1.881 Å and 101.8°, respectively. The Sr–O distances exhibit a much larger variation in ε-$SrTeO_3$, ranging from 2.350(8) to 2.964(7) Å. This difference originates from the three-dimensional nature of the $[SrO_3]_\infty$ framework which induces strong distortion of the strontium-oxygen polyhedra. In fact, the $[SrO_3]_\infty$ framework (Fig. 6a) can be described as built up of distorted edge-sharing $[SrO_7]$ polyhedra that are best described as monocapped SrO_6 octahedra with one considerably longer Sr–O distance. This 3-D framework delimits small tunnels running along the b-axis where the Te^{4+} cations reside (Fig. 6b). The

---

‡ The structure of $BaTeO_3(H_2O)$ was originally described in the non-standard setting $P2_1/a$ of space group no. 14. For better comparison with the structure of ε-$SrTeO_3$, we chose the standard setting in $P2_1/c$ for description of the $SrTeO_3(H_2O)$ structure.

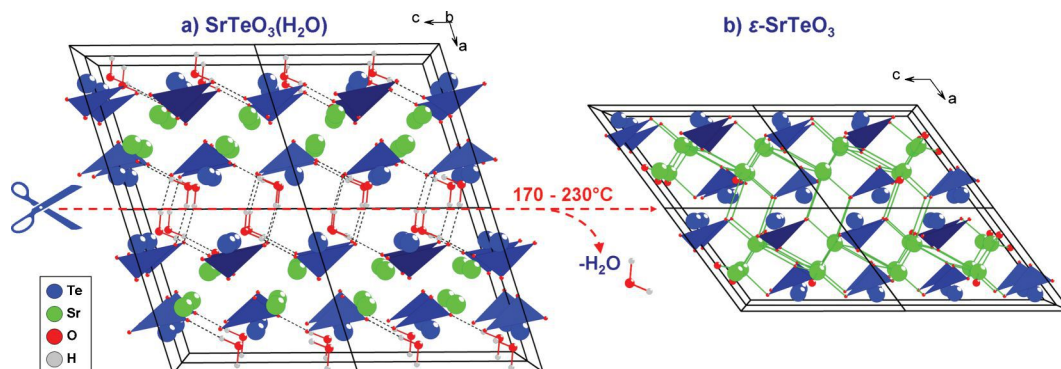**Fig. 4** The crystal structures of $SrTeO_3(H_2O)$ (a) and of ε-$SrTeO_3$ (b) in projections along their b-axes. The $[TeO_3]$ units are displayed as blue polyhedra and O–H$\cdots$O hydrogen bonding interactions are shown as dashed lines.
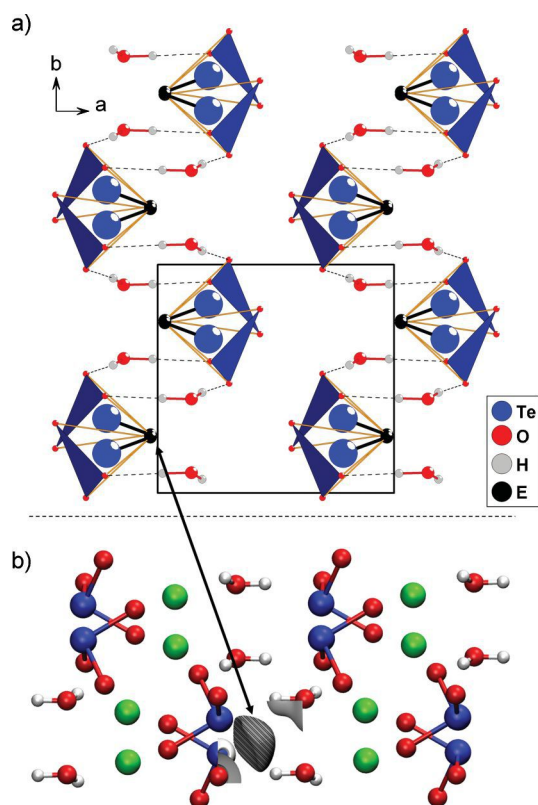
Fig. 5 a) Distribution of the ψ-[TeO$_3$E] tetrahedra in SrTeO$_3$(H$_2$O) viewed in a projection along the *c*-axis; b) 3-D plot of the ELF with a isovalue of 0.75 along the *c*-axis.

main structural set-up of ε-SrTeO$_3$ is related to that of the four previously reported SrTeO$_3$ polymorphs, where irregular [SrO$_n$] polyhedra (*n* = 6,7,8) share corners or faces and are further connected to isolated trigonal-pyramidal TeO$_3$ units *via* edge-sharing. The resulting channels have slightly different sizes and shapes and also provide the required space for the lone-electron pairs within the structures.[10–13]
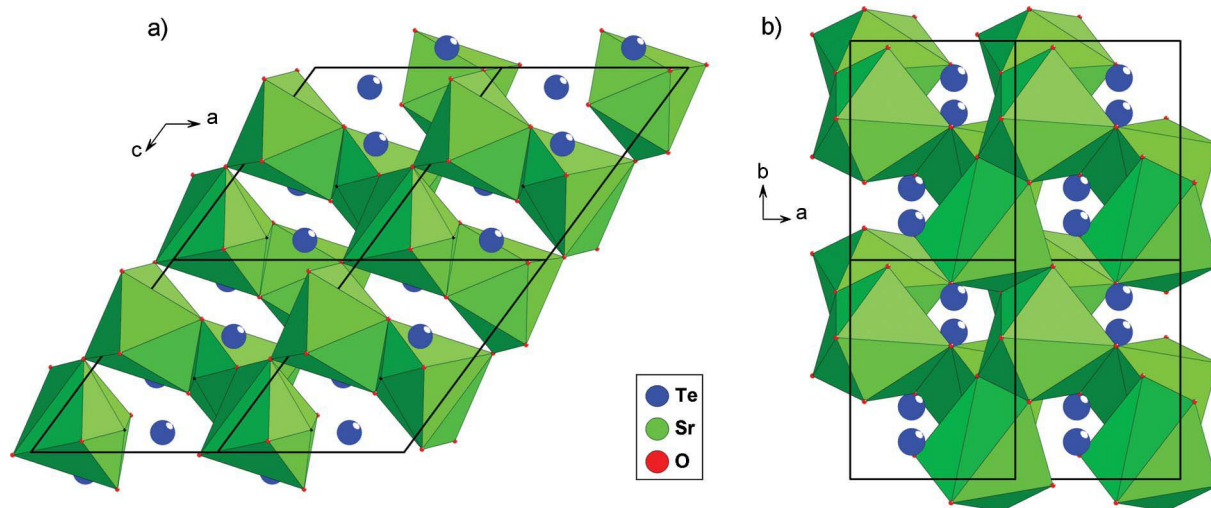
Compared with SrTeO$_3$(H$_2$O), the electronic lone pair in ε-SrTeO$_3$ was localised at a shorter distance of 1.38 Å from the tellurium atom, but likewise points out close to the [100] direction: Te-*E* = 0.23481*a* + 0.07147*b* + 0.09576*c*. Moreover, the calculated electronic charge increases to 2.65 electrons within a slightly smaller volume of 16.6 Å^3. Like in SrTeO$_3$(H$_2$O), the ψ-[TeO$_3$E] tetrahedra are isolated and form double rows running along the *c*-axis with two different orientations of the "O$_3$" basal plane (Fig. 7a). A view of the assembly of the ψ-[TeO$_3$E] tetrahedra along [101] shows the orientation of the electronic lone pairs of Te^{4+} in this structure (Fig. 7b).

For both SrTeO$_3$(H$_2$O) and ε-SrTeO$_3$ structures, the bond valence sums[43] were calculated with the parameters provided by Brese and O'Keeffe.[44] As can be seen in Table 6, the individual bond valence sums for each of the comparable atoms are very similar (except the water molecule which behaves differently) and are close to the expected value of 2 valence units (v.u.) for Sr, 4 v.u. for Te and 2 v.u. for the O atoms.

3.2 Thermal Behaviour

Two batches of microcrystalline SrTeO$_3$(H$_2$O), prepared by precipitation as well as by microwave-assisted hydrothermal synthesis, were subjected to thermal analysis measurements.

SrTeO$_3$(H$_2$O) starts to decomposes above 150 °C under elimination of the water molecule and subsequent crystallisation of ε-SrTeO$_3$, identified by the endothermic DSC effect and *in situ* powder X-ray diffraction (Fig. 8, 9). The observed mass losses of 6.95% of the precipitated and of 6.61% of the hydrothermally synthesized material are in reasonable agreement with the theoretical value of 6.41%. The slightly higher experimental values are most likely caused by adsorbed water.

Differences in onset temperatures, both in the TG and DSC experiments, pertain to the different crystallite size of the products from the two batches. The precipitated product presents a smaller crystallite thickness as showed in Fig. 1, and the water molecule is released at slightly lower temperatures than in the corresponding hydrothermally prepared product. The TG/DSC onsets for the
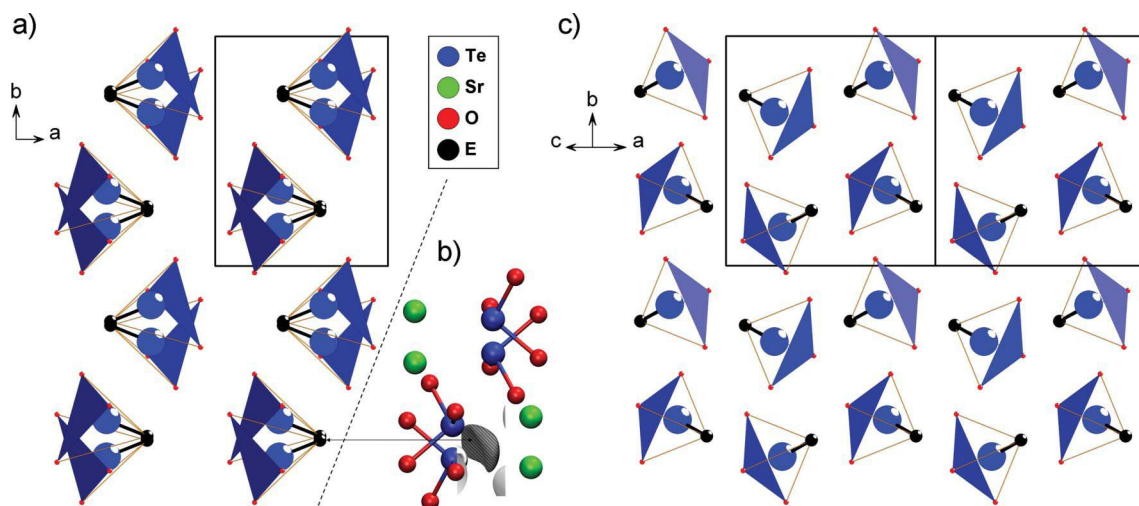

Fig. 6 ε-SrTeO$_3$: a) three-dimensional framework of [SrO$_3$]$_\infty$ built up of corner- and edge-sharing SrO$_7$ polyhedra along the *b*-axis; b) three-dimensional framework of [SrO$_3$]$_\infty$ forming small tunnels running along the *c*-axis where the Te^{4+} cations are situated.

Fig. 7 Distribution of the ψ-[TeO₃E] tetrahedra in ε-SrTeO₃: a) along the *c*-axis, forming double rows; c) along the [101] direction showing the electron lone pairs *E* of the Te⁴⁺ atoms alternatively oriented up and down; b) 3-D plot of the ELF with a isovalue of 0.75 along the *c*-axis.

Table 6 SrTeO₃(H₂O) and ε-SrTeO₃. Individual bond valence sums (v.u.)

SrTeO₃(H₂O)		ε-SrTeO₃	
Te	4.06	Te	4.19
Sr	2.02	Sr	2.01
O1	2.16	O1	2.15
O2	2.15	O2	2.22
O3	1.96	O3	1.83
OW	2.36		
HW1	1.34		
HW2	1.21		

Bond valence parameters: Te–O: $R_0 = 1.97$ Å; $B = 0.37$ Å; H–O: $R_0 = 0.907$ Å; $B = 0.28$ Å for d (H–O) $\not<$ 1.05 Å Sr–O: $R_0 = 2.118$ Å; $B = 0.37$ Å H–O: $R_0 = 0.990$ Å; $B = 0.59$ Å for d (H–O) $\not>$ 1.70 Å. Bond valence = $\exp((R_0 - R)/B)$.

precipitated material are 149 °C/173 °C and the TG/DSC onsets for the hydrothermally prepared material are 161 °C/215 °C; the peak maxima for both measurements are quite similar with 308 °C for the precipitated material and 319 °C for the hydrothermally prepared compound. The temperature-dependent X-ray measurements reveal transformations into the anhydrous phase above 170 °C for both samples.

Another endothermic effect corresponding to a phase transition of the ε-SrTeO₃ polymorph is observed for both samples with onsets at 580 °C for the precipitated material and at 594 °C for the hydrothermally prepared material. This phase transition is clearly visible in the temperature-dependent X-ray diffraction patterns for both samples above 570 °C. The broadening of the reflection peak widths and a decrease of the intensities are characteristic for a loss of crystallinity of the formed phases. These features, together with the similarity of the individual diffraction patterns of the four other polymorphs (α - δ) of SrTeO₃, make it very difficult to unambiguously assign the obtained phases. Nevertheless, some differences in the resulting powder patterns of the two samples are obvious. For both samples metastable ε-SrTeO₃ is transformed primarily into δ-SrTeO₃,[13] plus small amounts of α-SrTeO₃ (II)[10] for the original precipitated material and of γ-SrTeO₃ (II)[12] for
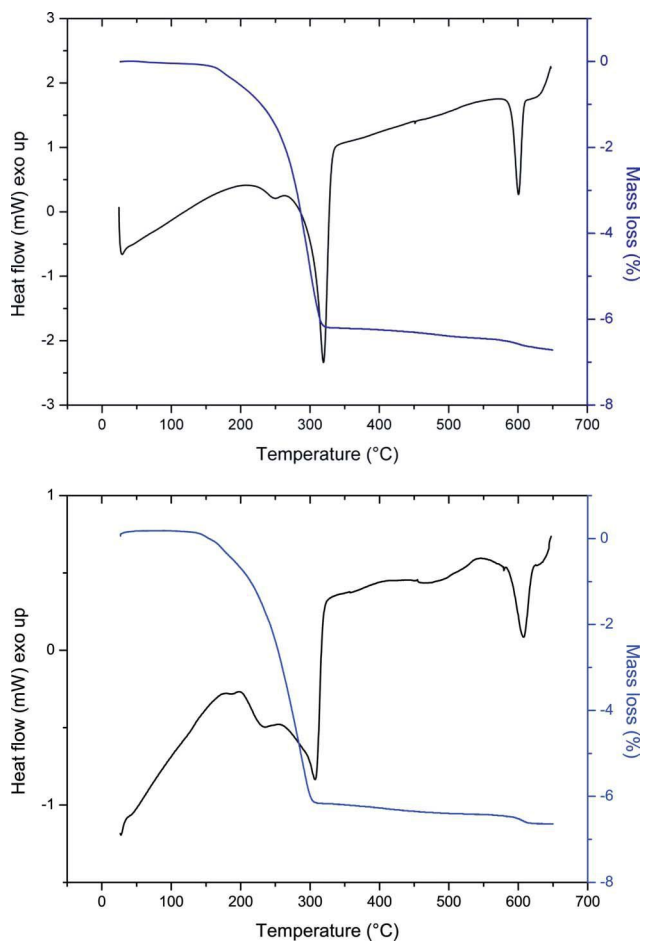

Fig. 8 TG (blue) and DSC (black) curves of hydrothermally prepared SrTeO₃(H₂O) (top) and of precipitated SrTeO₃(H₂O) (bottom).

the hydrothermally prepared material. We ascribe the observed differences in phase formation likewise to the different crystallite sizes of the original materials.
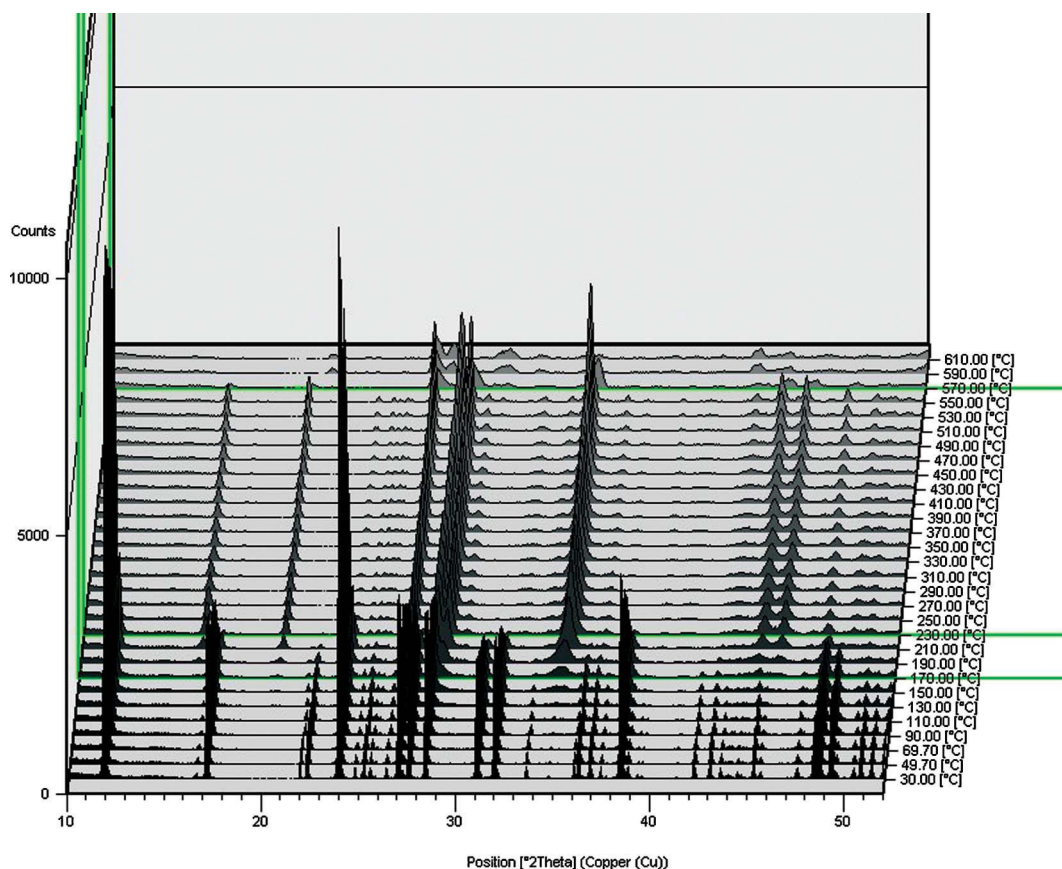
Fig. 9 Powder X-ray diffraction diagrams recorded between 30 and 610 °C of the hydrothermally prepared SrTeO₃(H₂O) sample. The green lines at 170 °C and 230 °C show the beginning and the end of the dehydration process of SrTeO₃(H₂O); the green line 570 °C shows the beginning of the phase transition of ε-SrTeO₃ into δ-SrTeO₃.

3.3 Vibrational spectroscopy of SrTeO₃(H₂O)

In the free state, the isolated trigonal-pyramidal [TeO₃²⁻] anion possesses C_{3v} symmetry and its fundamental vibrations have been assigned from Raman measurements in solution, as follows: symmetric stretching (ν_1, A₁) = 758 cm⁻¹, symmetric bending (ν_2, A₁) = 364 cm⁻¹, antisymmetric stretching (ν_3, E) = 703 cm⁻¹, antisymmetric bending (ν_4, E) = 326 cm⁻¹.[45] The four vibrational modes are active in both the Raman and IR spectra.[46]

For the analysis of the spectra of microcrystalline SrTeO₃(H₂O), we have performed a factor-group analysis of the unit cell,[46–48] on the basis of the described structure, correlating the symmetry of the "free" anion (C_{3v}), its site symmetry (C_1) and its factor group (C_{2h}). The results of this analysis are presented in Table 7. As can be seen in the crystalline compound, all degeneracies are removed

and all vibrational modes originate from four components, two active in the infrared and the other two in the Raman spectrum.

The FTIR spectrum in the spectral range between 1600 and 400 cm⁻¹ is shown in Fig. 10 and the Raman spectrum in the 1000–200 cm⁻¹ range in Fig. 11. The proposed band assignments are presented in Table 8 and briefly commented, as follows:

The stretching vibrations of the water molecule (not shown in Fig. 9) generate a very broad feature centred at 2962 cm⁻¹, with a relatively broad and undefined shoulder at *ca.* 3230 cm⁻¹. The position of this band confirms the existence of relatively short and moderate hydrogen bonds[45,49] with O⋯O separations of 2.703(3) and 2.781(3) Å, respectively. On the other hand, the water deformational mode, found at 1479 cm⁻¹ in the IR spectrum, presents an unusually low value.[50] Finally, in the low energy spectral range we have tentatively assigned the medium intensity

Table 7 SrTeO₃(H₂O). Factor group analysis of the TeO₃²⁻ vibrations ($P2_1/c$ (C_{2h}) and $Z = 4$)[a]

Vibrational mode	"Free" ion/C_{3v}	Site symm./C_1	Factor group/C_{2h}
Symm. stretching (ν_1)	A₁	A	Aₘ + Bₘ + Aᵤ + Bᵤ
Symm. bending (ν_2)	A₁	A	Aₘ + Bₘ + Aᵤ + Bᵤ
Antisymm. stretching (ν_3)	E	2A	Aₘ + Bₘ + Aᵤ + Bᵤ
Antisymm. bending (ν_4)	E	2A	Aₘ + Bₘ + Aᵤ + Bᵤ

[a] Activity under factor-group symmetry: Aₘ, Bₘ: Raman active; Aᵤ, Bᵤ: IR active.

Table 8 SrTeO$_3$(H$_2$O). Assignment of the bands in the vibrational spectra (band positions in cm^{-1})

Infrared	Raman	Assignment
ca. 3230 sh,br; 2962 s		ν (O–H) H$_2$O
1479 m		δ(H$_2$O)
855 w, 833 m	823 w, 759 vs	ν_s(TeO$_3$) (ν_1)
755 sh, 687 vs	727 w, 695 s	ν_{as}(TeO$_3$) (ν_3)
399 w, 357 s	355 w	δ_s(TeO$_3$) (ν_2)
323 vw	310 m	δ_{as}(TeO$_3$) (ν_4)
291 m	282 vw, 270 vw	ν_L(H$_2$O)
241s, 238 s, 232s	238 w	See text
212 vw, 202 w	205 vw	See text

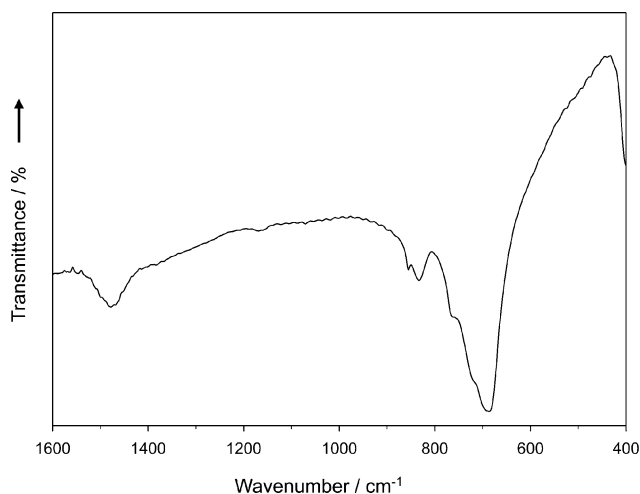vs: very strong; s: strong; m: medium; w: weak; vw: very weak; br: broad; sh: shoulder
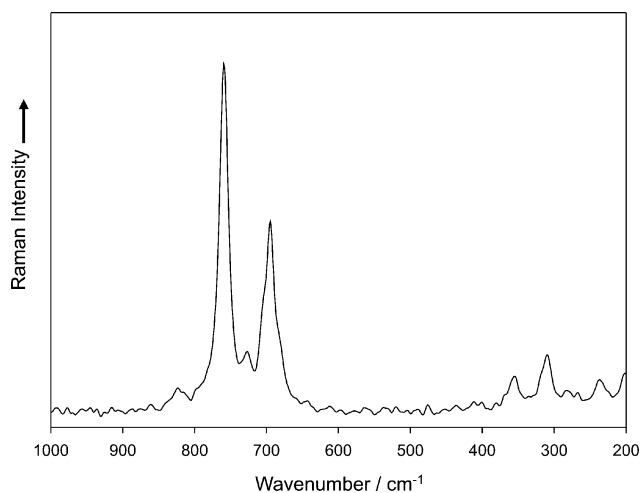

Fig. 10 FTIR spectrum of SrTeO$_3$(H$_2$O).

Fig. 11 Raman spectrum of SrTeO$_3$(H$_2$O).

IR band at 291 cm^{-1} and the two weak Raman signals at 282 and 270 cm^{-1} to librational modes of the water molecule.

In the region of the stretching vibrations all eight predicted bands could be clearly identified. A comparison of corresponding IR and Raman bands shows some energy differences, as expected from the fact that these bands originate in phonons of different parity (*cf.* Table 7). Besides, these differences are considered as a valuable criterion for the evaluation of the strength of coupling effects in the unit cell[51,52] and show that these effects are relatively important in the present case. Interestingly, the overall Raman pattern of SrTeO$_3$(H$_2$O) in this region shows a certain resemblance to that of the recently reported Raman spectrum of the mineral teineite, CuTeO$_3$·2H$_2$O.[53]

In the case of the TeO$_3^{2-}$ deformational modes the factor group expectations are not totally fulfilled, probably due to the relatively low intensity of the involved bands. The expected splitting is only observed for the ν_2-mode in the IR spectrum. On the other hand, both vibrations (ν_2 and ν_4) are particularly weak in the Raman spectrum, as also observed in the case of teineite.[53]

The groups of bands found below 250 cm^{-1} can surely by assigned to external (lattice) vibrations.

Acknowledgements

References

1 T. Yamada and H. Iwasaki, *Appl. Phys. Lett.*, 1972, **21**, 89–90.

2 T. Yamada, *Rev. Electr. Comm. Lab.*, 1975, **23**, 564–568.

3 R. Rai, S. Sharma and R. N. P. Choudhary, *J. Mater. Sci. Lett.*, 2002, **21**, 297–299.

4 T. Yamada and H. Iwasaki, *J. Appl. Phys.*, 1973, **44**, 3934–3939; A. Simon, R. Von der Mühll, J. Ravez, P. Hagenmuller and J. F. Pascual, *Mater. Res. Bull.*, 1979, **14**, 27–32.

5 A. Yu. Kudzin and L. Ya. Sadovskaya, *Iz. Vys. Ucheb. Zaved., Fizika*, 1977, **20**, 158.

6 I. H. Ismailzade, A. Yu. Kudzin and L. Ya. Sadovskaya, *Phys. Status Solidi*, 1979, **A52**, K105–K109.

7 V. P. Avramenko, A. Yu. Kudzin and L. Ya. Sadovskaya, *Ukrain. Fiz. Zhur.*, 1982, **27**, 556–560.

8 S. A. Malyutin, K. K. Samplavskaya and M. Kh. Karapet'yants, *Zh. Neorg. Khim.*, 1971, **16**, 1504–1507; G. Liberts and L. Ya. Sadovskaya, *Phys. Status Solidi*, 1980, **A62**, K167–K168; A. Yu. Kudzin, V. N. Moiseenko and L. Ya. Sadovskaya, *Fiz. Tver. Tela*, 1982, **24**, 2837–2839; H. G. Burckhardt, M. Koçak, N. Külcü and M. Trömel, *J. Solid State Chem.*, 1984, **54**, 256–259; Y. Elerman, *Doga: Turk. J. Phys.*, 1993, **17**, 465–473; S. N. Tripathi, R. Mishra, M. D. Mathews and P. N. Namboordiri, *Powder Diffr.*, 2001, **16**, 205–211.

9 B. Stöger, M. Weil, E. Zobetz and G. Giester, *Acta Crystallogr., Sect. B: Struct. Sci.*, 2009, **65**, 167–181.

10 O. A. Dityat'yev, P. S. Berdonosov, V. A. Dolgikh, D. W. Aldous and P. Lightfoot, *Solid State Sci.*, 2006, **8**, 830–835; V. E. Zavodnik, S. A. Ivanov and A. I. Stash, *Acta Crystallogr., Sect. E: Struct. Rep. Online*, 2007, **63**, i75–i76.

11 V. E. Zavodnik, S. A. Ivanov and A. I. Stash, *Acta Crystallogr., Sect. E: Struct. Rep. Online*, 2007, **63**, i111–i112.

12 V. E. Zavodnik, S. A. Ivanov and A. I. Stash, *Acta Crystallogr., Sect. E: Struct. Rep. Online*, 2007, **63**, i151.

13 V. E. Zavodnik, S. A. Ivanov and A. I. Stash, *Acta Crystallogr., Sect. E: Struct. Rep. Online*, 2008, **64**, i52.

14 J. Gopalakrishnan, *Chem. Mater.*, 1995, **7**, 1265–1275.

15 E. A. Ivankova, K. K. Samplavskaya, M. Kh. Karapet'yants and S. A. Malyutin, *Izv. Akad. Nauk SSSR, Neorg. Mater.*, 1966, **2**, 896–898.

16 E. A. Ivankova, K. K. Samplavskaya and M. Kh. Karapet'yants, *Iz. Akad. Nauk, Neorg. Mater.*, 1967, **3**, 1712–1714.

17 O. A. Dytyatyev and V. A. Dolgikh, *Mater. Res. Bull.*, 1999, **34**, 733–740.

18 H. G. Burckhardt and M. Trömel, *Acta Crystallogr., Sect. C: Cryst. Struct. Commun.*, 1983, **39**, 1322–1323.

19 D. Hottentot and B. O. Loopstra, *Acta Crystallogr., Sect. B: Struct. Crystallogr. Cryst. Chem.*, 1979, **35**, 728–729; J. Lapasse and J. Moret, *Acta Crystallogr., Sect. C: Cryst. Struct. Commun.*, 1985, **41**, 1558–1562.

20 N. Barrier, S. Malo, O. Hernandez, M. Hervieu and B. Raveau, *J. Solid State Chem.*, 2006, **179**, 3484–3488; M. Weil and B. Stöger, *Acta Crystallogr., Sect. E: Struct. Rep. Online*, 2007, **63**, i116–i118.

21 G. Brauer, editor, *Handbuch der Präparativen Anorganischen Chemie*, Band I, p. 437. Ferdinand Enke Verlag, Stuttgart, 1975.

22 P. Stadelmann, *Ultramicroscopy*, 1987, **21**, 131–145.

23 Bruker, *SMART and SAINT*, Bruker AXS Inc, Madison, Wisconsin, USA, 2005.

24 Bruker, *SADABS*, Bruker AXS Inc., Madison, Wisconsin, USA, 2005.

25 G. M. Sheldrick, *Acta Crystallogr., Sect. A: Found. Crystallogr.*, 2007, **64**, 112–122.

26 V. Petříček, M. Dušek and L. Palatinus, *JANA2006*, Institute of Physics, Praha, Czech Republic, 2006.

27 A. Le Bail, H. Duroy and J. L. Fourquet, *Mater. Res. Bull.*, 1988, **23**, 447–452.

28 K. Brandenburg and H. Putz, *Endeavour*, 2010. Crystal Impact GbR, Bonn.

29 W. A. Dollase, *J. Appl. Crystallogr.*, 1986, **19**, 267–272; A. March, *Z. Kristallogr.*, 1932, **81**, 285–297.

30 P. Stephens, *J. Appl. Crystallogr.*, 1999, **32**, 281–289.

31 L. W. Finger, D. E. Cox and A. P. Jephcoat, *J. Appl. Crystallogr.*, 1994, **27**, 892–900.

32 K. Brandenburg, *DIAMOND*, 2005, Crystal Impact GbR, Bonn, Germany.

33 R. Dovesi, V. R. Saunders, R. Roetti, R. Orlando, C. M. Zicovich-Wilson, F. Pascale, B. Civalleri, K. Doll, N. M. Harrison, I. J. Bush, P. D'Arco and M. Llunell, *CRYSTAL06*, User's Manual, University of Torino, Italy, 2006.

34 K. A. Peterson, D. Figgen, E. Goll, H. Stoll and M. Dolg, *J. Chem. Phys.*, 2003, **119**, 11113–11123.

35 S. Piskunov, E. Heifets, R. I. Eglitis and G. Borstel, *Comput. Mater. Sci.*, 2004, **29**, 165–178.

36 C. Gatti, V. R. Saunders and C. Roetti, *J. Chem. Phys.*, 1994, **101**, 10686–10696.

37 J. Contreras-Garcıa, A. Martın Pendas, J. M. Recio and B. Silvi, *J. Chem. Theory Comput.*, 2009, **5**, 164–173.

38 W. Humphrey, A. Dalke and K. Schulten, "VMD - Visual Molecular Dynamics", *J. Mol. Graphics*, 1996, **14**, 33–38.

39 B. Rottensten Nielsen, R. Grønbek Hazell and S. E. Rasmussen, *Acta Chem. Scand.*, 1971, **25**, 3037–3042.

40 R. D. Shannon, *Acta Crystallogr., Sect. A: Cryst. Phys., Diffr., Theor. Gen. Crystallogr.*, 1976, **32**, 751–767.

41 J. Zemann, *Monatsh. Chem.*, 1971, **102**, 1209–1216.

42 V. A. Dolgikh, *Russ. J. Inorg. Chem. (Eng. Transl.)*, 1991, **36**, 1117–1729; B. Kratochvfil and L. Jenfiovskfi, *Chem. Listy*, 1986, **80**, 575–585; J. Loub, *Collect. Czech. Chem. Commun.*, 1993, **58**, 1717–1738.

43 I. D. Brown, *The Chemical Bond in Inorganic Chemistry: The Bond Valence Model*, IUCr Monographs on Crystallography; I. D. Brown, *J. Appl. Crystallogr.*, 1996, **29**, 479–480.

44 N. E. Brese and M. O'Keeffe, *Acta Crystallogr., Sect. B: Struct. Sci.*, 1991, **47**, 192–197.

45 H. Siebert, *Anwendungen der Schwingungsspektroskopie in der Anorganischen Chemie*, Springer, Berlin, 1966.

46 S. D. Ross, *Inorganic Infrared and Raman Spectra*, McGraw-Hill, London, 1972.

47 A. Müller, E. J. Baran and R. O. Carter, *Struct. Bonding*, 1976, **26**, 81–139.

48 A. Fadini and F. M. Schnepel, *Vibrational Spectroscopy. Methods and Applications*, Ellis Horwood Ltd., Chichester, 1989.

49 E. Libowitzky, *Monatsh. Chem.*, 1999, **130**, 1047–1059.

50 H. D. Lutz, *Struct. Bonding*, 1988, **69**, 97–125.

51 A. Müller, *Z. Naturforsch.*, 1966, **21a**, 433–436.

52 E. J. Baran, E. G. Ferrer, I. Bueno and C. Parada, *J. Raman Spectrosc.*, 1990, **21**, 27–30.

53 R. L. Frost and E. C. Keeffe, *J. Raman Spectrosc.*, 2009, **40**, 128–132.